



Article

ZnO Films from Thermal Oxidation of Zn Films: Effect of the Thickness of the Precursor Films on the Structural, Morphological, and Optical Properties of the Products

Oswaldo Sánchez-Dena ^{1,2}, Susana Hernández-López ¹ , Marco Antonio Camacho-López ¹,
Pedro Estanislao Acuña-Ávila ³, Jorge Alejandro Reyes-Esqueda ⁴ and Enrique Viguera-Santiago ^{1,*} 

- ¹ Laboratorio de Investigación y Desarrollo de Materiales Avanzados (LIDMA), Facultad de Química, Universidad Autónoma del Estado de México, Campus el Rosedal, km 14.5 Carretera Toluca-Atzacmulco, Toluca 50200, México; oswaldo.sanchez@conacyt.mx (O.S.-D.); shernandezl@uaemex.mx (S.H.-L.); macamacholo@uaemex.mx (M.A.C.-L.)
- ² CONACyT Consejo Nacional de Ciencia y Tecnología. Av. Insurgentes Sur 1582, Col. Crédito Constructor, Benito Juárez, México City 03940, México
- ³ Departamento de Nanotecnología, Universidad Tecnológica de Zinacantepec, Zinacantepec 51361, México; pedro.avila@utzin.edu.mx
- ⁴ Instituto de Física, Universidad Nacional Autónoma de México, Circuito de la Investigación Científica, Ciudad Universitaria, México City 04510, México; reyes@fisica.unam.mx
- * Correspondence: eviguerass@uaemex.mx; Tel.: +52-72-2217-5109



Citation: Sánchez-Dena, O.; Hernández-López, S.; Camacho-López, M.A.; Acuña-Ávila, P.E.; Reyes-Esqueda, J.A.; Viguera-Santiago, E. ZnO Films from Thermal Oxidation of Zn Films: Effect of the Thickness of the Precursor Films on the Structural, Morphological, and Optical Properties of the Products. *Crystals* **2022**, *12*, 528. <https://doi.org/10.3390/cryst12040528>

Academic Editors: Wei Xu, Honglong Ning and Hua Zheng

Received: 26 February 2022

Accepted: 7 April 2022

Published: 10 April 2022

Publisher's Note: MDPI stays neutral with regard to jurisdictional claims in published maps and institutional affiliations.



Copyright: © 2022 by the authors. Licensee MDPI, Basel, Switzerland. This article is an open access article distributed under the terms and conditions of the Creative Commons Attribution (CC BY) license (<https://creativecommons.org/licenses/by/4.0/>).

Abstract: Zinc oxide (ZnO) films with different structural, morphological, and optical properties were obtained by (fixed) thermal oxidation of deposited metallic zinc (Zn) films. The main characteristics of the oxidized films are discussed in terms of the Zn film thickness. On-axis preferential crystallographic oriented growth of ZnO can be tuned based on the control of the thickness of the deposited Zn: *c*-axis (*a*-axis) for the thinnest (thicker) Zn film. The thicker ZnO film is rather *a*-textured, whereas the grains hosted by the ZnO films corresponding to the Zn films of intermediate thicknesses are more randomly oriented. For Zn films of ever-increasing thickness, a tendency towards the crystallization of larger ZnO nanocrystals holds, combined with a continuous increment on the surface roughness. In contrast, the fundamental bandgap of the resultant oxide-based films decreases with thickness. The roughness of the ZnO films is not directly measured. It is qualitatively described by the analysis of Zn-film micrographs obtained by Scanning Electron Microscopy and by the demonstration of strong optical scattering interactions present in the thicker ZnO films by their random lasing activity.

Keywords: zinc oxide; thin films; thermal oxidation

1. Introduction

Zinc oxide (ZnO) is a prominent material with high thermal and mechanical stability, capable of hosting several physical mechanisms and processes of practical use in photo-assisted catalysis, solar cells, blue and ultraviolet (UV) light-emitting diodes, UV lasers and sensor devices, thin-film transistors, transparent electrodes, hydrogen storage, piezoelectric transistors, varistors, phosphors, surface acoustic wave devices, display, touch panels, and flexible devices [1–7]. No less important is large-scale fabrication based on this semiconductor that includes sunscreens, ointments, and creams which assist wound healing, preservatives used in the food packaging industry [8,9], as well as the development of other biomedical applications [10–12]. ZnO has been pinpointed as the likely richest family of nanostructures [13]. Its versatility in crystallizing with practically any thinkable morphology (nanorods, nanorings, nanosprings, nanodisks, etc.) may be univocally related to the many means available to produce it [6,14–16].

Regarding the production of polycrystalline films in particular, the approach of synthesis comprising the subsequent thermal oxidation of metallic zinc films or layers obtained

by different deposition methods has shown to be an efficient route for the obtention of high-quality and reproducible nanostructured ZnO [6,17–26]. It is a simple method of preparation that discards the employment of expensive reagents and costly equipment while avoiding organic contamination by minimizing chemical waste and the release of toxic gases to the atmosphere. Although the method is simple and cheap, this route of synthesis has, surprisingly, rarely been adopted thus far, especially when glass substrates and thermal evaporation are used for the deposition of metallic zinc [4,6]. Furthermore, no general trend or systematic study can be found in the currently available literature regarding the parameters of Zn deposition in relation to the resultant characteristics of the ZnO films. While most authors report a *c*-axis preferential crystallographic orientation (PCO) under a given thermal treatment, others either report *a*-axis PCO or no PCO at all. On the other hand, using thermal evaporation, Zhao et al. (2004) encountered difficulties in depositing Zn directly on Si (111) substrates where very thin Au layers of 5 nm were deposited initially. Singh and Chakrabarti (2013) did not encounter such difficulties on Si (100) substrates [19,24].

Generally, previous investigations primarily employ the variation of the synthesis temperature and focus on the experimental conditions under which the better crystallinity of the ZnO films is attained. In this work, wurtzite ZnO films were prepared by thermal oxidation of metallic zinc films which were deposited on glass substrates by high-vacuum thermal evaporation. The crystal structure, morphology, and optical absorption properties of the produced films are discussed in terms of the morphology and the thickness of the precursor Zn metal films. Specifically, here it is shown that the thickness of the Zn metal films (50–600 nm) has a direct influence on the PCO or self-texture crystallization of ZnO, and on its global fundamental bandgap and scattering optical properties.

Since the oxidation annealing was kept fixed through temperature, time, and flow rate, the results can be effectively discussed in terms of this sole parameter. Here, it is presumed that the effects associated with the morphology and the size of the deposited Zn hexagonal-nanodisks are circumscribed to the thicknesses of the Zn films. The effect of the thickness of ZnO films on their polycrystalline characteristics and optical properties has been properly addressed by earlier studies, but in instances where the ZnO films were synthesized by other approaches that do not involve a subsequent thermal oxidation of the metallic Zn [27,28]. ZnO growth by thermal oxidation of Zn metal films is quite distinct since this procedure conveys an alternative method of synthesis capable of tuning the overall properties of the resultant films and may soon gain fundamental and practical interest due the paramount results presented in ref. [4].

2. Materials and Methods

Metallic Zn powder (98% purity) from Aldrich-Sigma (México) was used as starting reagent. Evaporation was performed using an Intercovamex T12 (Morelos, México) high-vacuum system: a 50 mg measure of Zn powder was placed in a molybdenum boat. When the pressure of the vacuum chamber was pumped down to 10^{-6} Torr, the Zn powder was heated by an electrical current with a rate of 10 Amp/min until 124 Amp was reached. In turn, zinc vapor was generated and condensed onto clean glass substrates placed 88 mm from the source. The first sample (labeled A1) was retrieved when the unaided eye observed a metallic shine. The deposition procedure was then reinitiated, allowing deposition time to last for 3, 6, and 10 additional minutes from this “shining” point. Subsequently, samples were designated 3 M, 6 M, and 10 M, respectively.

In the second stage of synthesis, the four samples were oxidized at 500 °C for 10 min. Such experimental condition was obtained from calorimetric–isothermal analysis at 500 °C under an oxygen atmosphere. After the depositions of metallic Zn, the material adhered to the inner walls of the vacuum system was collected and used for thermal analysis. An SDT Q600 from TA Instruments (USA) differential scanning calorimetry (DSC) device coupled to thermogravimetry (TGA) was used to determine the oxidation time and temperature. The calorimeter was calibrated to the indium and zinc melting points of 156.6 and 419.5 °C,

respectively. The samples were then analyzed in a wide temperature range between room temperature and 800 °C at a heating rate of 20 °C/min under an industrial-grade-oxygen atmosphere.

The resultant thicknesses of the metallic Zn and ZnO films were measured using a DEKTAK IIA profilometer. Structural and morphology characterizations were made using X-ray diffraction (XRD) on Bragg–Brentano Bruker D-8 Advance geometry with a source of $\text{CuK}\alpha$, 0.1541 nm radiation (Bruker, Linxeye, Karlsruhe, Germany), and JEOL JSM-6510LV (Mitaka, Tokyo, Japan) scanning electron microscopy at an acceleration voltage of 30 kV, respectively. In random lasing experiments, the unfocused 355 nm line of a PL2143A laser system by EKSPLA (Vilnius, Lithuania) featuring 26 ps pulses was used as the pumping source, and detection of the photoluminescence signal centered at 390 nm was made with an Ocean Optics Dual Channel SD2000 UV–visible spectrophotometer. Lastly, the combined effect of optical absorption due to the glass substrates plus the ZnO films was measured with a Cary 5000 UV-Vis-NIR spectrophotometer (USA). Experiments were performed at normal incidence on the surface of the samples.

3. Results and Discussion

ZnO films were obtained after thermal oxidation of the Zn metal films. Figure 1 displays (a) the gain in weight as the Zn is oxidized to ZnO, and (b) an enlarged view of the XRD patterns around $2\theta = 35^\circ$. At the isotherm $T = 500^\circ\text{C}$, complete oxidation with 24% maximal weight gain is achieved after 10 min. The percentage agrees with stoichiometry/molar calculations. Bragg reflections comprise only peaks of the hexagonal wurtzite crystal structure with lattice constants $a = b = 0.326\text{ nm}$ and $c = 0.522\text{ nm}$ (JCPDS card no. 36-1451). The c/a ratio (1.106) is slightly smaller compared to that of the ideal wurtzite ($\sqrt{8/3} = 1.633$), indicating the formation of the stable crystal structure of ZnO [29]. No indication of metallic Zn is evident after the thermal oxidations. The XRD data of the Zn films (not shown, see for example, Figures 5 and 6 in ref. [18]) were matched with the JCPDS card no. 65-3358, denoting polycrystalline grains with a hexagonal close packed crystal lattice ($a = b = 0.266\text{ nm}$, $c = 0.49\text{ nm}$). The resultant ZnO films feature a tunable behavior regarding preferential crystallographic orientation (PCO). As shown in Figure 1b, the one corresponding to the thinnest Zn metal film (50 nm, sample A1Ox) presents c -axis PCO based on stronger reflection in the 0001 plane, $2\theta = 34.46^\circ$. In contrast, a clear transition towards a -axis PCO based on stronger reflection in the $10\bar{1}0$ plane, $2\theta = 31.85^\circ$, can be noticed for the ZnO film obtained after application of the same thermal oxidation treatment to the thickest Zn metal film (600 nm, sample 10MOx). The tendency of the ZnO grains growing with a specific crystallographic direction normal to the substrate seems to diminish for the intermediate cases of Zn films with thicknesses of 280 and 350 nm, samples 3MOx and 6MOx, respectively.

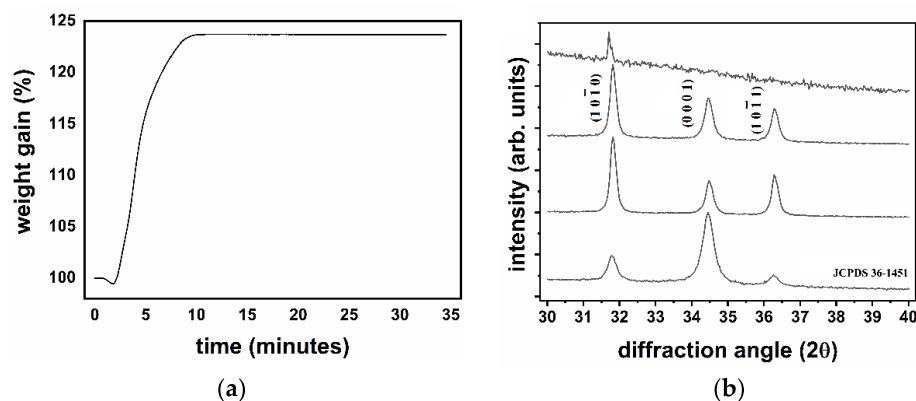


Figure 1. (a) Isothermal TGA analysis of metallic Zn at 500 °C; (b) XRD results: changes in the position and breadth of the main Bragg peak indicate a tuning of the on-axis preferential crystallographic orientation, as well as of the average size of the ZnO nanocrystals.

Fanni et al. (2014) have previously composed a schematic representation of the hexagonal structure presenting the two extreme cases of PCO, *a*-textured versus *c*-textured. They have also reported the corresponding XRD patterns in a broad 2θ : 30–70° range [27]. Both are here reproduced in Figure 2 to aid the discussion of our results. Texture, refers to the extreme case in which all the grains have crystallized predominantly along a specific direction. PCO is a more appropriate term to denote several intermediate cases that precede texture, that is, when only a high percentage of the grains effectively grow with such orientation. More rigorously, the term ‘self-texture’ would be employed if grain growth is known to be non-epitaxial [30,31]. More succinctly, self-texture is evident if the “textured structure caused by the film itself without influence of the substrate” [7], as is generally accepted for ZnO films supported on glass substrates [32–34].

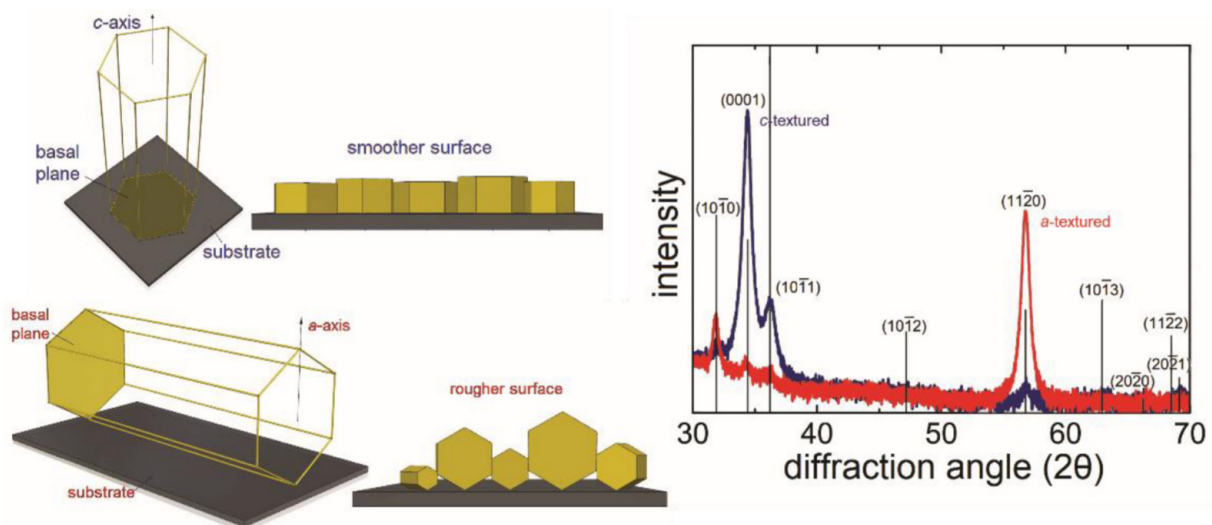


Figure 2. Schematic representation of the geometrical configurations and their corresponding X-ray diffraction patterns of *c*- and *a*-textured ZnO films. Adapted with permission from ref. [27]. Copyright Year 2014 Elsevier.

Based on Figure 2, it can be stated that the film A1Ox exhibits a strong *c*-axis PCO and that the *a*-axis PCO characteristics shown by film 10MOx represent an earlier stage of *a*-axis texture development. These PCO characteristics are evidenced by lack of reflections from other crystallographic planes seen in the entire sampled range 2θ : 30–80°. Note the absence of the particularly strong diffraction peak shown c.a. $2\theta = 57^\circ$ in Figure 2. Furthermore, the lone peak corresponding to the reflection on plane (10 $\bar{1}$ 0) of film 10MOx is significantly smaller in intensity when compared to those observed in the other samples, and it does not feature a single Lorentzian-shape peak. Rather, it contains a contribution arising from the overlapping of at least two very close peaks.

This possibly indicates that the observed reflection depicts the weighted average of distinct diffraction contributions which are very close to each other, and possibly arise from grains with different orientations within a common plane perpendicular to the normal component of the *a*-axis PCO substrate. This line of argument or picture will be reinforced when the morphological results for the Zn and the ZnO films are presented. Meanwhile, to address the rate at which the PCO is established for each studied ZnO film, the relative degree of orientation or texture coefficient (TC) can be quantitatively assessed for a generic plane (*abcd*) by means of the following formula [35,36]:

$$TC(abcd) = \frac{I(abcd)}{I_{PDF}(abcd)} \frac{1}{\sum_{(hkl)=1}^N \frac{I(hkl)}{I_{PDF}(hkl)}} \quad (1)$$

In Equation (1), $I(abcd)$ is the normalized intensity measured for the reflection plane of interest, the main diffraction peak in each sample. $I_{PDF}(abcd)$ is the corresponding normalized standard intensity for ZnO powders indicated in the Powder Diffraction Data, PDF files, card no. 36-1451 in this case. N is the number of reflection planes considered in the calculation. $N = 3$ in this case for planes $(10\bar{1}0)$, (0001) , and $(10\bar{1}1)$. Powders composed of completely randomly distributed grains are described by $TC \approx 1$. The value increases for polycrystalline films with PCO, and converges to N for highly textured films. The results are presented in Table 1. Additionally, the estimated averaged ZnO grain sizes and the measured thicknesses of both Zn and ZnO films are also listed. The averaged grain sizes (D) are estimated from analysis of the XRD patterns using the Scherrer's formula [37,38]:

$$D = \frac{0.9\lambda}{\beta \cos \theta} \quad (2)$$

where $\lambda = 1.5406 \text{ \AA}$ and $\beta = B - b$. B is the observed Full Width at Half Maximum (FWHM) of the main diffraction peak. $b = 0.07$ is the contribution to the line broadening due to the instrument as extracted from the XRD measurement of a lanthanum hexaboride (LaB_6) single crystal.

Table 1. Relevant structural and morphological parameters of the produced ZnO films in terms of the thickness of the precursor metallic Zn films. TC: Texture coefficient calculated by Equation (1). D : average grain size calculated by Equation (2).

Sample	Zn Film Thickness (nm)	ZnO Film Thickness (nm)	TC ($abcd$)	D (nm)
A1Ox	50	50	(0001):2.0	27
3MOx	280	420	($10\bar{1}0$):1.6	68
6MOx	350	480	($10\bar{1}0$):1.5	58
10MOx	600	610	($10\bar{1}0$):3.0	413

In all instances, the B values were determined after resolution of the three XRD peaks by fitting to Lorentzian functions and using the 'Multiple Peak Fit' tool from OriginLab software (version Pro2019b). The extracted w values from the fittings have been assumed to be the FWHM values according to the specifications found in the 'Function Dialog' of the software. In the case of sample 10MOx, the lone diffraction peak corresponding to the reflection on plane $(10\bar{1}0)$ was resolved into two overlapping components, giving $w_1 = FWHM_1 = 0.05$ and $w_2 = FWHM_2 = 0.04$. The combined effect was used for the calculation of D , that is, $B_{(10\bar{1}0)-10MOx} = w_1 + w_2 = 0.09$. The value $2\theta = 31.75^\circ$ also represents the middle position between the centers of the two overlapped peaks. Similarly, the overlapping of peaks was taken into consideration for the calculation of $TC_{(10\bar{1}0)-10MOx} = 3.0$. Instead of equating $I(10\bar{1}0)$ to 1, $I(10\bar{1}0) = 0.91 = I(10\bar{1}0)_{\text{peak2}} + (I(10\bar{1}0)_{\text{peak1}} - I(10\bar{1}0)_{\text{peak2}})/2 = 0.82 + (1 - 0.82)/2$ were used. See the attached Figure A1 in the Appendix A.

A linear relationship holds between the thicknesses of the precursor Zn films and those of the produced ZnO films. Given that the thermal oxidation treatments were kept fixed, this implies that the former is the main parameter influencing the final structural characteristics. Since the only variable introduced in the deposition of metallic Zn is the time of deposition, control of the degree of PCO of ZnO films can be effectively achieved in a rather simple manner using this synthesis technique. By close inspection of Table 1, there seem to exist certain Zn film thickness prerequisites for the development of a given PCO. It can be argued that the development of a c -axis PCO (c -PCO) is favored when Zn metal films of the order of ≤ 50 nm are employed.

On the other hand, Zn metal films with thicknesses between 500 and 600 nm seem to be needed to produce ZnO films with a significant a -axis PCO (a -PCO). Fanni et al. (2014) have introduced the concept of 'selection layer' to denote the initial regions of ZnO growth with a c - or $-a$ -axis texture in terms of a minimum thickness of the ZnO film. With films

deposited by low-pressure metalorganic chemical vapor deposition, they found that *c*-axis texture can be promoted regardless of thickness down to the order of <50 nm. Conversely, *a*-axis texture can only be achieved for ZnO films thicker than 250 nm [27]. Shia and Huang (2004) prepared several ZnO films with thicknesses ranging from 200 to 600 nm using radio frequency magnetron sputtering and found a strong *c*-PCO for films with thickness less than 500 nm [28].

Clearly, the observed tendencies are highly dependent on the method of synthesis. Interestingly, a tendency which more closely resembles the one herein reported was observed with ZnO films prepared by atomic layer deposition [39]. Therein, strong *c*-, *c*-, and strong *a*-PCOs were observed for thicknesses of 40, 120, and 180 nm, respectively. Focusing on the production of ZnO films by subsequent oxidation of Zn metal films, it is observed that the method or atmosphere employed in the oxidation process is not critical. Thin Zn films have been deposited by thermal evaporation and then immersed in ionized water at a temperature of 90 °C for 16 h, i.e., wet oxidation [17]. The main diffraction peak for plane (0001) was also observed (*c*-PCO) for the ZnO film obtained after oxidation of a 50 nm-thick Zn metal film.

While results for 100–200 nm-thick metallic Zn film deposition using thermal evaporation and conventional thermal oxidation at 500 °C fixed adjust to findings reported in Table 1 [19], results obtained with 300 nm-thick Zn films deposited on Si (111) substrates do not [24]. The Zn–ZnO transformation induced by thermal oxidation of 250 nm-thick Zn films deposited on glass by thermal evaporation shows to be incomplete and complete with *c*-PCO when the oxidations were performed at 500 and 550 °C, respectively [6]. In contrast, Hoffmann et al. (2021) used another method of deposition of the Zn films and, regardless of the thickness of the pure metal layer within a 5–75 nm range, they observed preferential growth in the (10 $\bar{1}$ 0) direction, *a*-PCO [4].

The films were deposited on quartz substrates and oxidized at temperatures of 250, 350, and 450 °C. Likewise, Cho et al. (1999) in their pioneering work regarding the fabrication of ZnO films by oxidation of metallic Zn growth using DC sputtering on amorphous fused silica substrates. No PCO was observed for the ZnO coming from the oxidation at 500 °C of 200 nm thick Zn films [26]. Lastly, it is also worth noticing that when the ZnO films are used as seed layers for the obtention of vertically aligned nano-rods/wires, the on-axis PCO characteristics can either be inherited or not [4,39]. Particularly, it has been shown that the thickness of the initial metallic Zn layers has an impact on the structural, morphological, and optical properties of the ZnO nanowires [4].

Mostly, *c*-PCO has been reported, and its origin has been tacitly attributed to a minimization of the surface free energy taking place at the planes that lie among the hexagonal crystallographic planes [30,40–42]. However, PCO cannot be attributed simply to a single mechanism, as is discussed thoroughly in ref. [7] and in similar cited reports. The observed differences regarding the development of a certain type of on-axis PCO or texture can be synthesized in terms of the employed reaction conditions. The synthesis can be tuned by the presence of moisture at the oxidation stage and by the amount of residual oxygen present in the deposition of the metallic Zn [4]. Both the method of Zn deposition and the type of substrate are critical in the control of the structural characteristics of ZnO films obtained by oxidation of Zn films. When the method of deposition conveys only thermal evaporation, the experimental conditions seem to have a dominant influence rather than the oxidation process.

Despite the various inconsistencies or dissimilar trends discussed thus far, one can produce a consistent observation according to the consulted literature: ZnO films exhibiting *c*-PCO are characterized by smoother surfaces than those exhibiting *a*-PCO (Figure 2). On average, the reported roughness for both types of nanostructures are of the order of <10 and >70 nm, respectively [19,27,33–39]. Films without PCO are described by roughness of around 30–40 nm [26]. The roughness of the substrate is elsewhere signaled as a factor influencing the overall quality of the surfaces [33].

Figure 3 shows the observed morphology of the deposited Zn as a function of the film thickness. Perhaps no morphology can be resolved for sample A1, but well-defined hexagonal nanodisks are obtained for the additional 3-minutes-and-longer deposition times. In the former case (sample 3 M), the average size of the nanodisks is about 250 nm. Interestingly, the morphology is maintained as nanodisk size increases with deposition time up to approximately 1000 nm. The deposition of Zn nanodisks has been previously reported [43]; however, there are no reports regarding the formation of this morphology at earlier stages of deposition.

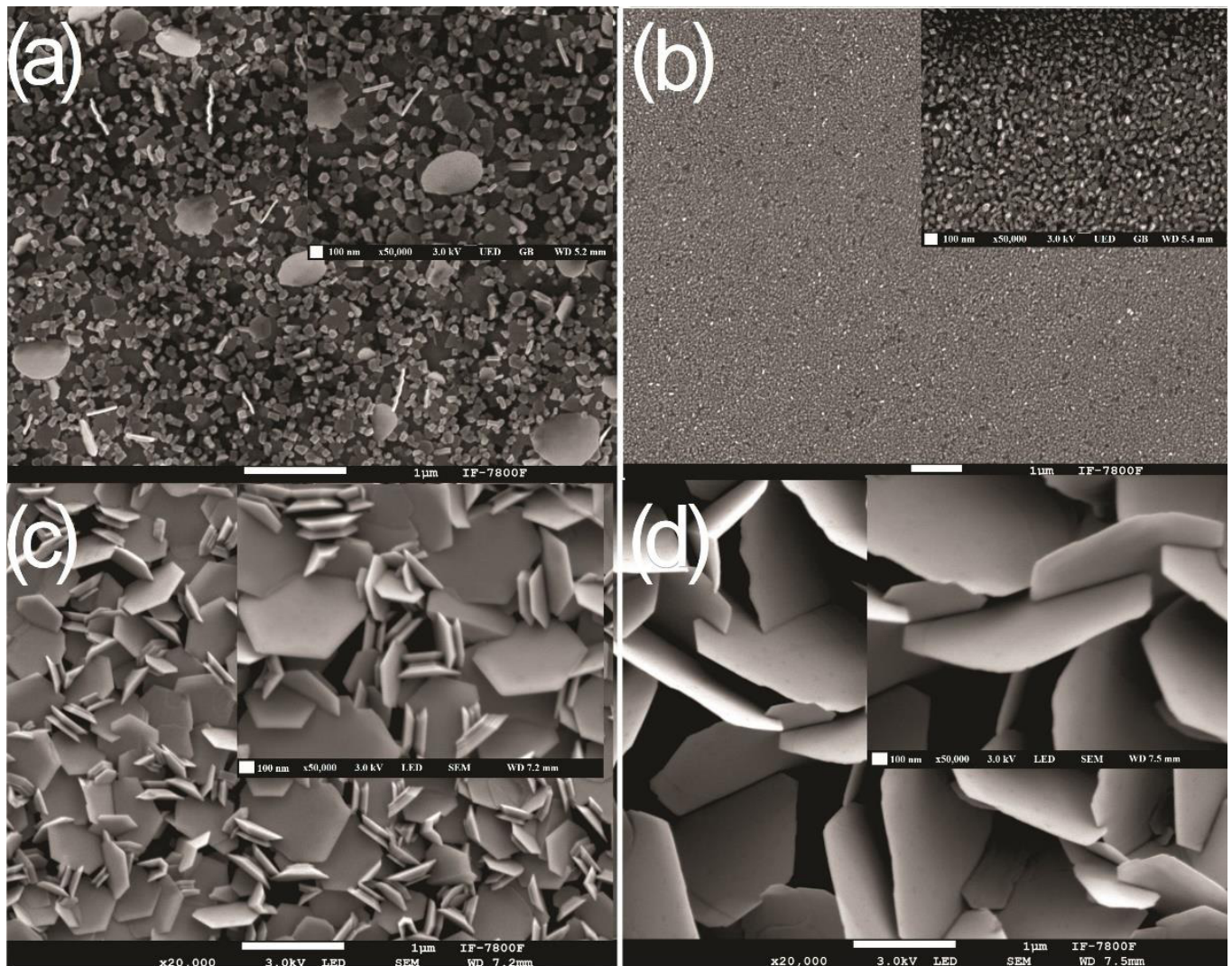


Figure 3. Micrographs of the Zn films, obtained with SEM under a fixed resolution ($\times 50,000$ for the inset figures). Four different samples with different average particle sizes: (a) A1 (50 nm); (b) 3 M (250 nm); (c) 6 M (350 nm); (d) 10 M (850 nm).

In the present investigation, no explicit evaluation of the roughness of the films is carried out. However, based on Figure 3, it can be indirectly stated that roughness tends to enlarge as the films thicken. The overall influence of the roughness of the Zn films on the final characteristics of the ZnO films can be deduced based on the initial thickness of the Zn films. In turn, the latter is critically influenced by the average size of the deposited nanodisks, as is shown by the nonlinear relationship in Figure 4.

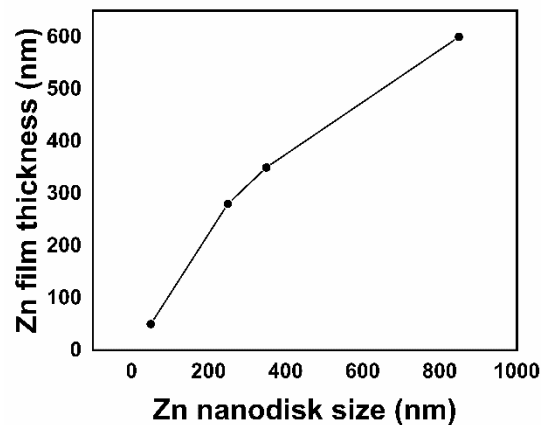


Figure 4. The relationship between the particle size and thickness of the deposited metallic Zn adjusts to a quadratic curve as the deposition time increases.

After Jaber and Laanab (2014), it is believed that an excess of thermal energy drives particle growth in the (0001) direction [44], as usually observed in the growth of ZnO. This point can be readily seen by the aid of the scanning electron microscopy (SEM) images shown in Figure 5. Whereas the supplied energy is mainly utilized in the growth of ZnO walls on the edges of the Zn particles for thicker Zn metallic films possessing larger nanodisks, for thinner films with smaller nanodisks, some of the surplus energy is utilized for the growth of ZnO along the normal to the edges as well. The morphology of the particles constituting the ZnO films is influenced by the initial morphology of the Zn nanodisks. Oxidation is favored at the vertices for the smaller Zn disks (Figure 5a), resulting in a ZnO nano-gearwheel. In the case of 3MOx (Figure 5b), both the density and the diameter of the disks increase, driving the growth of a nano-rice morphology with the axis of growth in the direction $(10\bar{1}0)$. ZnO needles supported on the edges of the precursor Zn nanodisks are formed, also in the direction $(10\bar{1}0)$, when the latter increase further in size (Figure 5c,d). The shape of the hexagonal plates is preserved.

The extreme case of the thicker ZnO film is of particular interest. Figure 5d shows that the needles have different orientations within a common plane. These orientations should be perpendicular to the normal component of the substrate in the development of an *a*-PCO or texture. This situation has been addressed earlier in the present discussion of results as the possible cause of XRD peak splitting into two overlapping contributions (Figure 1). The corresponding SEM micrograph of the Zn film (Figure 3d) shows that the plane containing the needles is not exactly perpendicular to the normal component of the substrate. Only a component of the overall orientation of the needles satisfies such physical instance and could be used to explain the rather low observed intensity of the XRD peak. The rather large dimensions of the off-normal-oriented needles are certainly a factor that aids in the observation of the lone Bragg reflection on plane $(10\bar{1}0)$.

Rougher surfaces scatter light more strongly than smoother surfaces. Above, only analysis of SEM images has been used to qualitatively describe the surface quality of the deposited metallic Zn films. Inheritance of the roughness characteristics of the ZnO films from those of the Zn films has also been implicitly presumed. Further evidence on behalf of such arguments can be found in data extracted from conventional random lasing experiments. For over twenty years, it has been well-known that ZnO nanostructures feature random lasing [45–50]. Random lasing denotes the enhanced emission of a material due to population inversion based on the localization of light, or light confinement by natural cavities made of randomly dispersed particles of high transparency. Usually, this is evidenced by a sharp line of photoluminescence. A prerequisite for random lasing is strong optical scattering [51–53], which is of importance for the samples studied in this work, especially for samples 6MOx and 10MOx. Strong optical scattering is indicated simply by their whiter color to the eye. Samples A1Ox and 3MOx are more transparent.

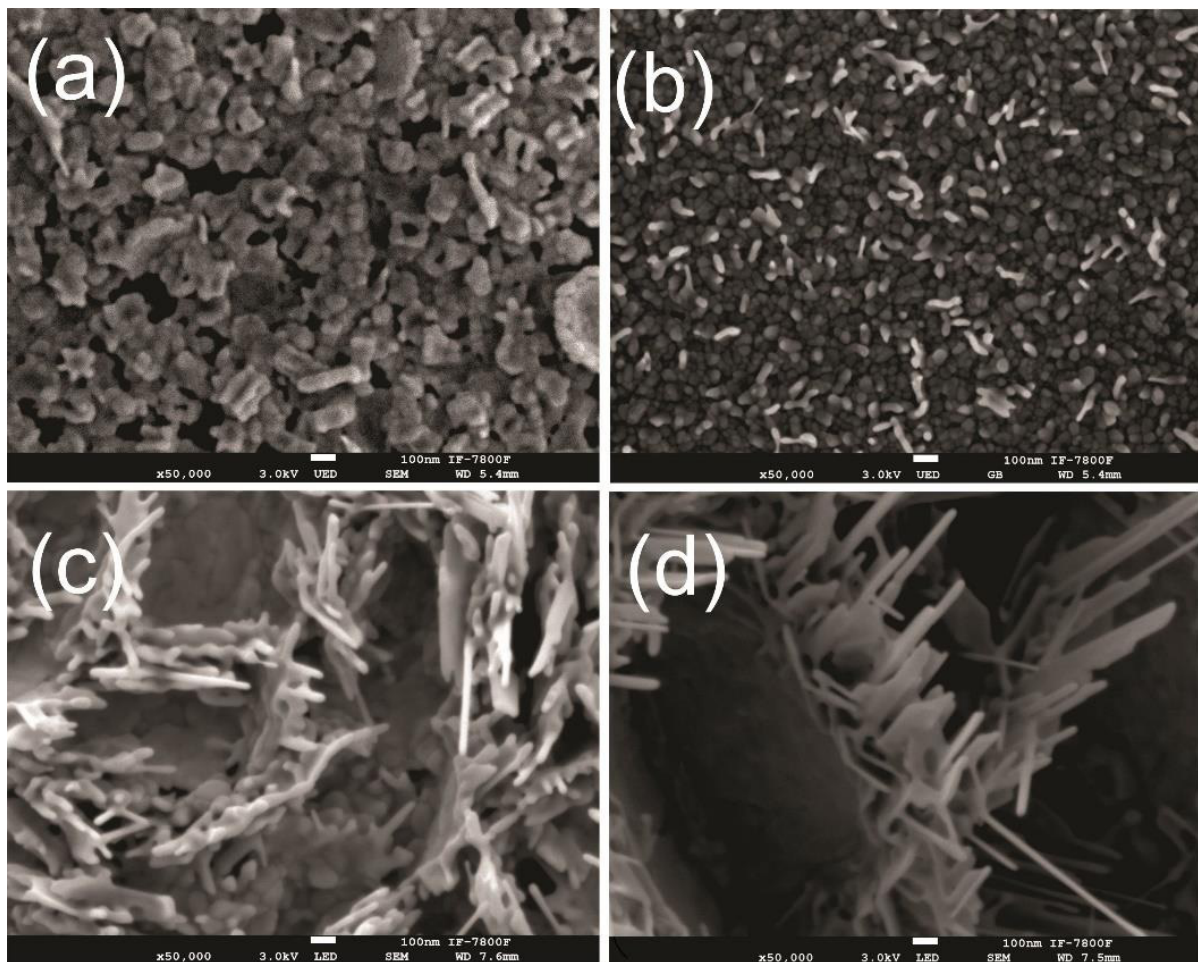


Figure 5. ZnO morphologies as a function of the Zn film thickness: (a) A1Ox; (b) 3MOx; (c) 6MOx; (d) 10MOx.

To prove the importance of this scattering effect, preliminary measurements of random lasing were performed as described in the Materials and Methods section. Figure 6 shows the intensity of the photoluminescence signal centered at 390 nm, as the pump energy is varied. In the figure, it is apparent that the signal begins to increase nonlinearly with the pumping intensity after the physical instance for the detected intensity, i.e., the lasing threshold. The signal increases more significantly for samples 6MOx and 10MOx due to stronger scattering effects compared to those featured in the other two thinner films. The present results bolster the reported convention that thicker ZnO films with *a*-PCO are characterized by rougher surfaces.

It should be emphasized that the initial roughness of the Zn films plays an important role in the structural and morphological developments of the ZnO films, as well as their optical properties. The effect of one on the others could only be traced by separation of the synthesis of the ZnO films into two stages of Zn deposition and subsequent thermal oxidation, and their corresponding characterizations.

Strong optical scattering is also responsible for the observed increase in absorbance and random lasing. In consideration of the four absorption curves shown in Figure 7, a red shift occurs as the thickness of the ZnO films increases as indicated by the local maxima located at 370 nm. For direct electronic transitions, the bandgap is proportional to the square of the absorption coefficient, and the bandgap value (E_g) is extracted from the determination of the fundamental absorption edge by extrapolation of the peak onset to the abscissa in eV units (the Tauc plot method). An example of the determination of E_g for sample A1Ox employing this method is shown in the inset of Figure 7.

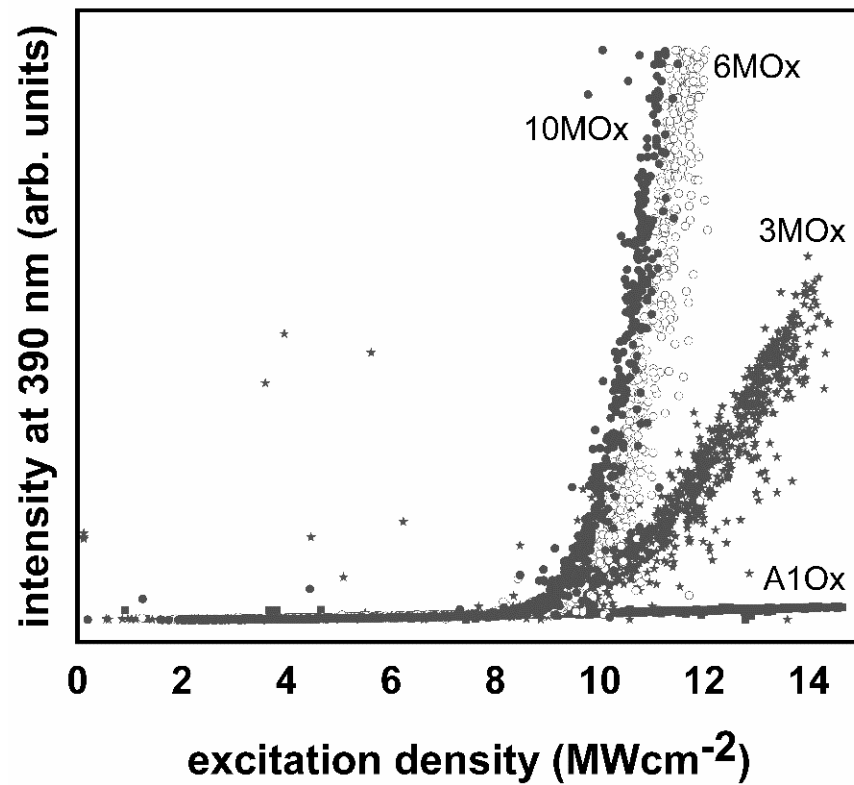


Figure 6. Random lasing probability: the photoluminescence signal of the four samples, centered at 390 nm, is collected in a reflection experimental configuration.

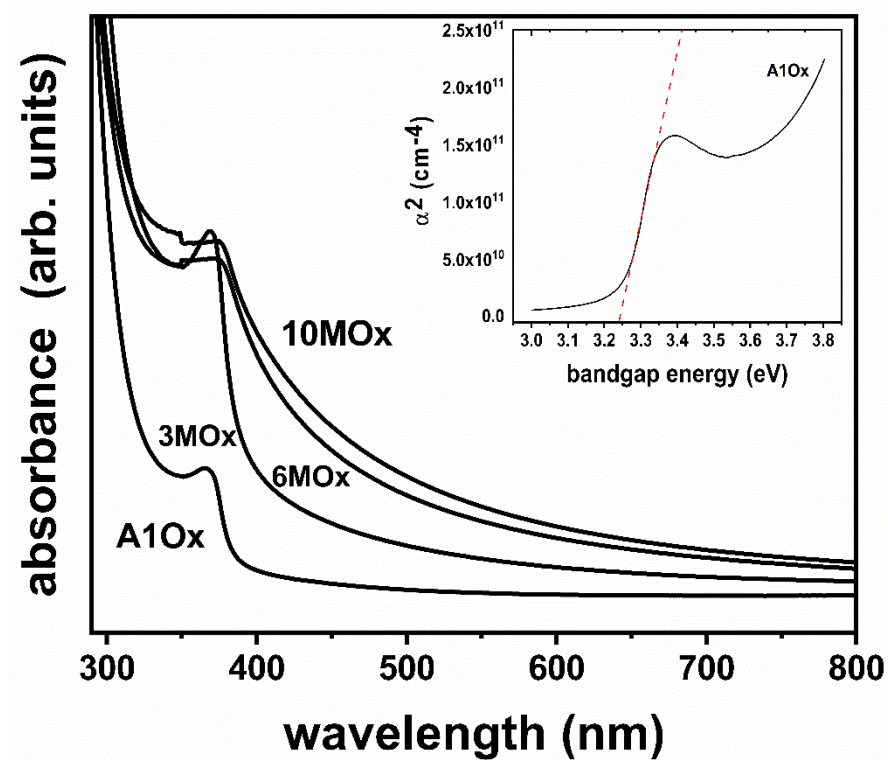


Figure 7. Absorption spectra of ZnO films. The Tauc plot used to determine the fundamental bandgap of sample A1Ox is shown in the inset. See Figure A2 in Appendix A for the Tauc plots of the rest of the samples.

Another approach for the determination of E_g has been developed by Meulenkamp (1998) [54,55]:

$$E_g = \frac{1240}{\lambda_{1/2}} \quad (3)$$

where $\lambda_{1/2}$ is the wavelength at which the absorption is half that at the excitonic peak or shoulder with local maxima located *ca.* 370 nm. The determined values of E_g by both approaches are given in Table 2; see the attached Figure A2 in the Appendix A. The agreement is good, within a margin of error bounded to the second significant figure. Nonetheless, these values should be taken with precaution because the absorption curves shown in Figure 7 do not correspond to the ZnO films alone, but rather to the system ZnO film plus substrate, for each studied sample. The measurements were made with the Cary 5000 UV-Vis-NIR spectrophotometer in absorbance mode, so that air was considered as the standard reference instead of a clean glass substrate. Yet because the fundamental absorption edge of glass is very close to that of ZnO, signal overlapping might be taking place and, thus, slight alteration of both the intensity and spectral features of the absorption of the ZnO films should not be neglected.

Table 2. Fundamental optical bandgaps of the ZnO films, determined by two distinct methods.

Sample	Tauc Plot Method (eV)	$\lambda_{1/2}$ Method (eV)
A1Ox	3.24	3.26
3MOx	3.18	3.21
6MOx	2.84	2.85
10MOx	2.78	2.78

The variation in bandgap with film thickness can be attributed to different mechanisms. First, based on the average grain sizes shown in Table 1, bandgap shifting due to quantum confinement is discarded, since the established upper size limit for these effects to be non-negligible is ~ 7 nm particle size [54,55]. Absorbance spectral shifting translates into bandgap shifting, and it is likely to rely more on the variation of populations of intrinsic defects such as oxygen vacancies (V_O) and zinc interstitials (Zn_i) [56,57]. Concomitant evidence can be found in the literature regarding this subject. Indeed, in their seminal paper, Srikant and Clarke showed that the nominal bandgap value for pure ZnO single crystals is $E_g = 3.3$ eV, and that other smaller values, usually reported for films and other sorts of polycrystalline ZnO, can be attributed to a valence band-donor transition [58]. The transition dominates optical absorption when the bulk of a single crystal is probed using conventional reflectance and transmission measurements rather than only its surface using spectroscopic ellipsometry. The volumetric populations of intrinsic defects in a single crystal are large when compared at the surface level.

On the other hand, the values presented in Table 2 imply a transition from semiconducting behavior towards a conducting behavior of the ZnO films as they thicken. Recently, based on novel experimental techniques, it has been demonstrated with similarly prepared films that the main intrinsic defect in ZnO is the larger structural entity or cluster $V_{Zn}-(V_O)_2$, caused by interaction between zinc vacancies and oxygen vacancies [4]. According to the same work, this type of defect cluster tends to increase the overall resistivity of the films while its concentration decreases at higher calcination temperatures. The highest calcination temperature utilizing thermal oxidation in ref. [4] is close to the one utilized in the present investigation. Hence, it can be inferred that the higher electron conductivity that could be possibly associated with samples 6MOx and 10MOx arises from higher population of $V_{Zn}-(V_O)_2$ clusters.

Lastly, a final comment is given regarding the possible role of optical scattering on the bandgap shifting. By close inspection of Figure 7 in the visible regime (400–700 nm), it can be noticed that stronger scattering interactions contribute to higher absorption rates, with perhaps optical extinction being a more suitable term. Both glass and ZnO films

are highly transparent, so that if not for the non-negligible scattering of photons, all the samples would show a common absorption baseline in this regime, as is the case for sample A1Ox. The effect should be intensified near the ultraviolet region for the same reason humans see a blue sky. No clear mechanism for the spectral shifting based on the very same arguments can now be envisioned. Absorption and scattering are extensive parameters that add up unequally to the overall optical extinction. In principle, if the intensity or strength differences are minimal between two close interactions, within a $\pm\Delta\lambda$ range which is additive, they overlap, resulting in spectral shifting. In other words, perhaps the strength of the optical scattering addressed to samples 6MOx and 10MOx is comparable to that of their optical absorption, so that it contributes to the large bandgap shifting registered in Table 2.

4. Conclusions

The approach of synthesis comprising high-vacuum thermal evaporation deposition and subsequent thermal oxidation of metallic zinc (Zn) is here demonstrated to be an efficient route for the fabrication of reproducible zinc oxide (ZnO) nanostructures. Recently, the available knowledge regarding the defect structure of thin ZnO films has been refined based on samples prepared by a similar method altogether with their involvement in the realization of stimulating applications [4]. Therein, Zn films were deposited by rf magnetron sputtering. In the present investigation, the separated characterization of the precursor Zn films and of the resultant ZnO films has permitted isolation of an important factor influencing the preferential crystallographic orientation (PCO) and texturizing effects extensively associated with ZnO. It has been demonstrated that on-axis PCO can be tuned by the deposition conditions of the metallic zinc. The thickness and particle size of the Zn films can be controlled with the deposition time. After a relatively soft thermal treatment of 500 °C for 10 min, ZnO films can be obtained with different structural characteristics and morphologies, influencing their optical properties. The changes in the optical absorption spectra have been recorded and their origin based on the combination of different possible mechanisms discussed. Future research by our group will be aimed to disentangle them and to identify which of these have a major role in the observed shifting of the fundamental absorption edge.

Author Contributions: Conceptualization, E.V.-S.; methodology, P.E.A.-Á.; validation, S.H.-L. and M.A.C.-L.; formal analysis, O.S.-D., S.H.-L., and M.A.C.-L.; investigation, O.S.-D. and P.E.A.-Á.; resources, E.V.-S.; data curation, O.S.-D. and S.H.-L.; writing—original draft preparation, O.S.-D. and P.E.A.-Á.; writing—review and editing, J.A.R.-E. and E.V.-S.; supervision, M.A.C.-L. and E.V.-S.; project administration, E.V.-S.; funding acquisition, J.A.R.-E. and E.V.-S. All authors have read and agreed to the published version of the manuscript.

Funding: This research was funded by CONACyT México, grant number A1-S-33899, and partially supported by DGAPA-UNAM IN112919.

Institutional Review Board Statement: Not applicable.

Informed Consent Statement: Not applicable.

Data Availability Statement: Not applicable.

Acknowledgments: Oswaldo Sánchez-Dena thanks the post-doctoral grant Cátedras COMECyT-Folio No. CAT2021-0096. The authors wish to acknowledge the technical assistance of Carlos Raúl Magaña Zavala, Diego Armando Quiterio, and Manuel Aguilar Franco (Laboratorio Central de Microscopía, Instituto de Física-UNAM). Alejandro Esparza García (ICAT-UNAM) and Alejandra Núñez Pineda (CCIQS UAEM-UNAM) assisted with the thickness measurements and support with calorimetry experiments, respectively. Acknowledgment is also given to Gabriel Alejandro Medel Méndez for his support with Figure 2 and final editing of other figures.

Conflicts of Interest: The authors declare no conflict of interest. The funders had no role in the design of the study; in the collection, analyses, or interpretation of data; in the writing of the manuscript, or in the decision to publish the results.

Appendix A

In the case of sample 10MOx, prior to the determination of the average ZnO grain size, the X-ray diffraction (XRD) peak corresponding to the reflection plane (10 $\bar{1}$ 0) was first resolved into two Lorentzian components, as shown in the following figure:

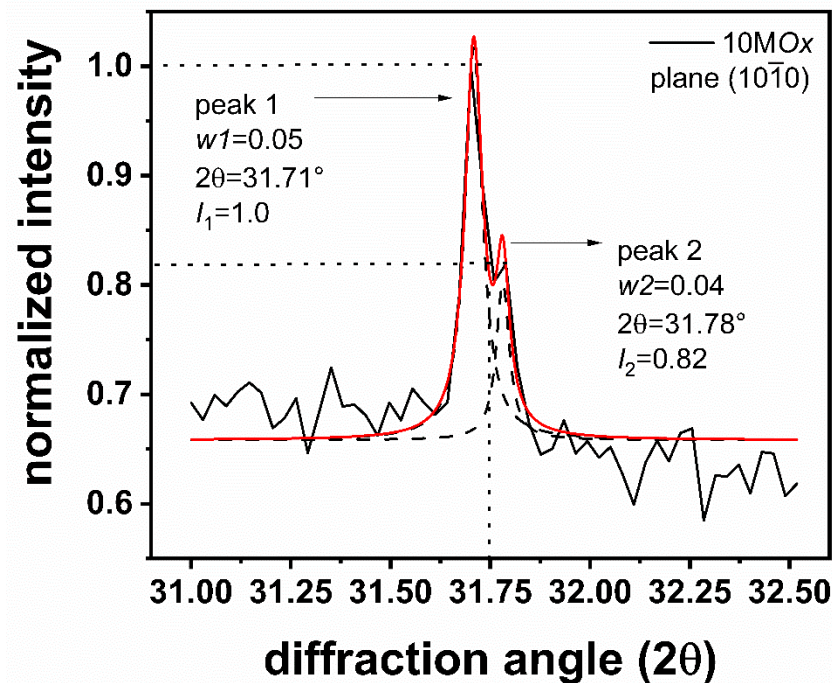


Figure A1. Enlarged view of the XRD pattern corresponding to ZnO film 10MOx, in the 2θ range 31.0–31.50°. Shown also are the fitted curves and the obtained fitting parameters, which were used to calculate the texture coefficient (TC) and average grain size (D) shown in Table 1.

The Tauc plots obtained for the determination of the fundamental bandgap for samples other than A1Ox are shown in the next figure:

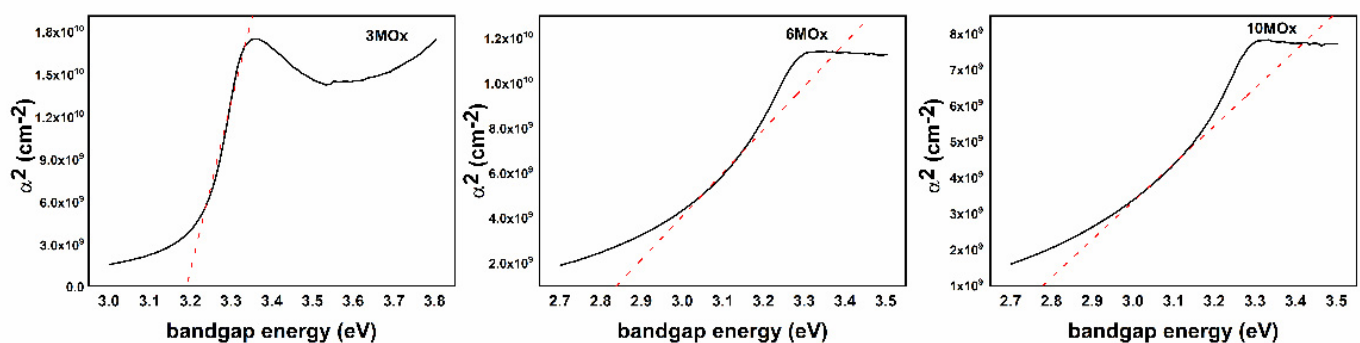


Figure A2. Tauc plots of samples 3MOx, 6MOx, and 10MOx, respectively.

References

1. Kazmierczak-Balata, A.; Grzadziel, L.; Guziewicz, M.; Venkatachalapathy, V.; Kutznetsov, A.; Krzywiecki, M. Correlations of thermal properties with grain structure, morphology, and defect balance in nanoscale polycrystalline ZnO films. *Appl. Surf. Sci.* **2021**, *546*, 149095. [[CrossRef](#)]
2. Samavati, A.; Awang, A.; Samavati, Z.; Ismail, A.F.; Othman, M.H.D.; Velashjerdi, M.; Eisaabadi, B.G.; Rostami, A. Influence of ZnO nanostructure configuration on tailoring the optical bandgap: Theory and experiment. *Mater. Sci. Eng. B* **2021**, *263*, 114811. [[CrossRef](#)]
3. Okada, T.; Tateyama, C.; Hoshino, K.; Kawashima, T.; Washio, K. Aluminum and vanadium co-doping effects on the optical and electrical properties of oriented ZnO films. *Mater. Res. Exp.* **2021**, *8*, 016402. [[CrossRef](#)]

4. Hoffmann, R.C.; Sanctis, S.; Liedke, M.O.; Butterling, M.; Wagner, A.; Njel, C.; Schneider, J.J. Zinc Oxide Defect Microstructure and Surface Chemistry Derived from Oxidation of Metallic Zinc: Thin-Film Transistor and Sensor Behavior of ZnO Films and Rods. *Chem. Eur. J.* **2021**, *27*, 5422–5431. [[CrossRef](#)]
5. Johar, M.A.; Afzal, R.A.; Alazba, A.A.; Manzoor, U. Photocatalysis and Bandgap Engineering Using ZnO Nanocomposites. *Adv. Mater. Sci. Eng.* **2015**, *2015*, 934587. [[CrossRef](#)]
6. Khanlary, M.R.; Vahedi, V.; Reyhani, A. Synthesis and Characterization of ZnO Nanowires by Thermal Oxidation of Zn Thin Films at Various Temperatures. *Molecules* **2012**, *17*, 5021–5029. [[CrossRef](#)]
7. Kajikawa, Y. Texture development of non-epitaxial polycrystalline ZnO films. *J. Cryst. Growth* **2006**, *289*, 387–394. [[CrossRef](#)]
8. Czyzowska, A.; Barbasz, A. A review: Zinc oxide nanoparticles –friends or enemies? *Int. J. Environ. Health Res.* **2020**, *2020*, 1805415. [[CrossRef](#)]
9. Perez Espitia, P.J.; Ferreira Soares, N.F.; dos Reis Coimbra, J.S.; de Andrade, N.J.; Souza Cruz, R.; Alves Medeiros, E.A. Zinc oxide nanoparticles: Synthesis, antimicrobial activity and food packaging applications. *Food Bioprocess Technol.* **2012**, *5*, 1447–1464. [[CrossRef](#)]
10. Singh, T.A.; Sharma, A.; Tejwan, N.; Ghosh, N.; Das, J.; Sil, P.C. A state of the art review on the synthesis, antibacterial, antioxidant, antidiabetic and tissue regeneration activities of zinc oxide nanoparticles. *Adv. Colloid Interface Sci.* **2021**, *295*, 102495. [[CrossRef](#)]
11. Jin, S.-E.; Jin, H.-E. Antimicrobial Activity of Zinc Oxide Nano/Microparticles and Their Combinations against Pathogenic Microorganisms for Biomedical Applications: From Physicochemical Characteristics to Pharmacological Aspects. *Nanomaterials* **2021**, *11*, 263. [[CrossRef](#)] [[PubMed](#)]
12. Mishra, P.K.; Mishra, H.; Ekielski, A.; Talegaonkar, S.; Vaidya, B. Zinc oxide nanoparticles: A promising nanomaterial for biomedical applications. *Drug Discov. Today* **2017**, *22*, 1825–1834. [[CrossRef](#)] [[PubMed](#)]
13. Wang, Z.L. Nanostructures of zinc oxide. *Mater. Today* **2004**, *7*, 26–33. [[CrossRef](#)]
14. Joraid, A.A.; Soleiman, A.S.; Al-Maghrabi, M.A.; Almutairy, M.H. Studies of crystallization kinetics and optical properties of ZnO films prepared by sol-gel technique. *J. Sol-Gel Sci. Technol.* **2021**, *97*, 523–539. [[CrossRef](#)]
15. Ul Haq, A.N.; Nadhman, A.; Ullah, I.; Mustafa, G.; Yasinzi, M.; Khan, I.J. Synthesis Approaches of Zinc Oxide Nanoparticles: The Dilemma of Ecotoxicity. *J. Nanomater.* **2017**, *2017*, 8510342. [[CrossRef](#)]
16. Kolodziejczak-Radzimska, A.; Jesionowski, T. Zinc Oxide—From Synthesis to Application: A Review. *Materials* **2014**, *7*, 2833–2881. [[CrossRef](#)]
17. Balela, M.D.L.; Pelicano, C.M.O.; Ty, J.D.; Yanagi, H. Formation of zinc oxide nanostructures by wet oxidation of vacuum deposited Zn thin film. *Opt. Quant. Electron.* **2017**, *49*, 3. [[CrossRef](#)]
18. Acuña-Avila, P.E.; López, R.; Viguera-Santiago, E.; Hernández-López, S.; Camacho-López, M.; Ornelas-Gutierrez, C.; Antunez, W. Effect of thermal treatment on Zn nanodisks. *AIP Adv.* **2015**, *5*, 067109. [[CrossRef](#)]
19. Singh, S.; Chakrabarti, P. Optical Characterization of ZnO Thin Films Grown by Thermal Oxidation of Metallic Zinc. *Adv. Sci. Eng. Med.* **2013**, *5*, 677–682. [[CrossRef](#)]
20. Zhang, D.; Wang, C.; Liu, Y.; Shi, Q.; Wang, W. High *c*-axis preferred orientation ZnO thin films prepared by oxidation of metallic zinc. *Opt. Laser Technol.* **2012**, *44*, 1136–1140. [[CrossRef](#)]
21. Dhananjay; Nagaraju, J.; Krupanidhi, S.B. Investigations on zinc oxide thin films grown on Si (1 0 0) by thermal oxidation. *Mater. Sci. Eng. B* **2007**, *137*, 126–130. [[CrossRef](#)]
22. Rusu, G.G.; Girtan, M.; Rusu, M. Preparation and characterization of ZnO thin films prepared by thermal oxidation of evaporated Zn thin films. *Superlattices Microstruct.* **2007**, *42*, 116–122. [[CrossRef](#)]
23. Li, Z.W.; Gao, W.; Reeves, R.J. Zinc oxide films by thermal oxidation of zinc thin films. *Surf. Coat. Technol.* **2005**, *198*, 319–323. [[CrossRef](#)]
24. Zhao, J.; Hu, L.; Wang, Z.; Zhao, Y.; Liang, X.; Wang, M. High-quality ZnO films prepared by low temperature oxidation of metallic zinc. *Appl. Surf. Sci.* **2004**, *229*, 311–315. [[CrossRef](#)]
25. Wang, Y.G.; Lau, S.P.; Lee, H.W.; Yu, S.F.; Tay, B.K.; Zhang, X.H.; Hng, H.H. Photoluminescence study of ZnO films prepared by thermal oxidation of Zn metallic films in air. *J. Appl. Phys.* **2003**, *94*, 354–358. [[CrossRef](#)]
26. Cho, S.; Ma, J.; Kim, Y.; Sun, Y.; Wong, G.K.L.; Ketterson, J.B. Photoluminescence and ultraviolet lasing of polycrystalline ZnO thin films prepared by the oxidation of the metallic Zn. *Appl. Phys. Lett.* **1999**, *75*, 2761–2763. [[CrossRef](#)]
27. Fanni, L.; Abersold, B.A.; Alexander, D.T.L.; Ding, L.; Morales Masis, M.; Nicolay, S.; Ballif, C. *c*-texture versus *a*-texture low pressure metalorganic chemical vapor deposition ZnO films: Lower resistivity despite smaller grain size. *Thin Solid Film.* **2014**, *565*, 1–6. [[CrossRef](#)]
28. Lin, S.-S.; Huang, J.-L. Effect of thickness on the structural and optical properties of ZnO films by r.f. magnetron sputtering. *Surf. Coat. Technol.* **2004**, *185*, 222–227. [[CrossRef](#)]
29. Morkoc, H.; Özgür, Ü. *Zinc Oxide: Fundamentals, Materials and Device Technology*; John Wiley and Sons: Danvers, MA, USA, 2009.
30. Fujimura, N.; Nishihara, T.; Goto, S.; Xu, J.; Ito, T. Control of preferred orientation for ZnO_x films: Control of self-texture. *J. Cryst. Growth* **1993**, *130*, 269–279. [[CrossRef](#)]
31. Goto, S.; Fujimura, N.; Nishihara, T.; Ito, T. Heteroepitaxy of zinc oxide films, considering non-epitaxial preferential orientation. *J. Cryst. Growth* **1991**, *115*, 816–820. [[CrossRef](#)]
32. Mekhnache, M.; Drici, A.; Hamideche, L.S.; Benzarouk, H.; Amara, A.; Cattin, L.; Bernede, J.C.; Guerioune, M. Properties of ZnO thin films deposited on (glass, ITO and ZnO:Al) substrates. *Superlattices Microstruct.* **2011**, *49*, 510–518. [[CrossRef](#)]

33. Prepelita, P.; Medianu, R.; Sbarcea, B.; Garoi, F.; Filipescu, M. The influence of using different substrates on the structural and optical characteristics of ZnO thin films. *Appl. Surf. Sci.* **2010**, *256*, 1807–1811. [[CrossRef](#)]
34. Triboulet, R.; Perriere, J. Epitaxial growth of ZnO films. *Prog. Cryst. Growth Charact. Mater.* **2003**, *47*, 65–138. [[CrossRef](#)]
35. Moutinho, H.R.; Hasoon, F.S.; Abulfotuh, F.; Kazmerski, L.L. Investigation of polycrystalline CdTe thin films deposited by physical vapor deposition, close spaced sublimation, and sputtering. *J. Vac. Sci. Technol. A* **1995**, *13*, 2877–2883. [[CrossRef](#)]
36. Harris, G.B. X. Quantitative measurement of preferred orientation in rolled uranium bars. *Lond. Edinb. Dublin Philos. Mag. J. Sci.* **1952**, *43*, 113–123. [[CrossRef](#)]
37. Percharsky, V.K.; Zavalij, P.Y. *Fundamentals of Powder Diffraction and Structural Characterization of Materials*, 2nd ed.; Springer: New York, NY, USA, 2009. [[CrossRef](#)]
38. Klug, H.P.; Alexander, L.E. *X-Ray Diffraction Procedures: For Polycrystalline and Amorphous Materials*, 2nd ed.; John Wiley and Sons: Danvers, MA, USA, 1974; ISBN 978-0-471-49369-3.
39. Solís-Palomar, F.; Martínez, E.; Meléndrez, M.F.; Pérez-Tijerina, E. Growth of vertically aligned ZnO nanorods using textured ZnO films. *Nanoscale Res. Lett.* **2011**, *6*, 524. [[CrossRef](#)] [[PubMed](#)]
40. Lee, H.S.; Lee, J.Y.; Kim, T.W.; Kim, D.W.; Cho, W.J. Formation mechanism of preferential c-axis oriented ZnO thin films grown on pi-Si substrates. *J. Mater. Sci.* **2004**, *39*, 3525–3528. [[CrossRef](#)]
41. Deng, H.; Russell, J.J.; Lamb, R.M.; Jiang, B.; Li, Y.; Zhou, X.Y. Microstructure control of ZnO thin films prepared by single source chemical vapor deposition. *Thin Solid Film.* **2004**, *458*, 43–46. [[CrossRef](#)]
42. Choi, J.H.; Tabata, H.; Kawai, T. Initial preferred growth in zinc oxide thin films on Si and amorphous substrates by a pulsed laser deposition. *J. Cryst. Growth* **2001**, *226*, 493–500. [[CrossRef](#)]
43. Devan, R.S.; Lin, J.-H.; Huang, Y.-J.; Yang, C.-C.; Wun, S.Y.; Liou, Y.; Ma, Y.-R. Two-dimensional single-crystalline Zn hexagonal nanoplates: Size-controllable synthesis and X-ray diffraction study. *Nanoscale* **2011**, *3*, 4339–4345. [[CrossRef](#)]
44. Jaber, B.; Laanab, L. One step synthesis of ZnO nanoparticles in free organic medium: Structural and optical characterizations. *Mater. Sci. Semicond. Process.* **2014**, *27*, 446–451. [[CrossRef](#)]
45. Wiersma, D.S. The physics and applications of random lasers. *Nat. Phys.* **2008**, *4*, 359–367. [[CrossRef](#)]
46. Torres-Torres, C.; Trejo-Valdez, M.; Sobral, H.; Santiago-Jacinto, P.; Reyes-Esqueda, J.A. Stimulated Emission and Optical Third-Order Nonlinearity in Li-Doped ZnO Nanorods. *J. Phys. Chem. C* **2009**, *113*, 13515–13521. [[CrossRef](#)]
47. Luan, F.; Gu, B.; Gomez, A.S.L.; Yong, K.-T.; Wen, S.; Prasad, P.N. Lasing in nanocomposite random media. *Nano Today* **2015**, *10*, 168–192. [[CrossRef](#)]
48. Yu, S.F.; Yuen, C.; Lau, S.P.; Lee, H.W. Zinc oxide thin-film random lasers on silicon substrate. *Appl. Phys. Lett.* **2004**, *84*, 3244–3246. [[CrossRef](#)]
49. Fallert, J.; Dietz, R.J.B.; Hauser, M.; Stelzl, F.; Klingshirn, C.; Kalt, H. Random lasing in ZnO nanocrystals. *J. Lumin.* **2009**, *129*, 1685–1688. [[CrossRef](#)]
50. Nakamura, T.; Firdaus, K.; Adachi, S. Electron-hole plasma lasing in a ZnO random laser. *Phys. Rev. B* **2012**, *86*, 205103. [[CrossRef](#)]
51. John, S. Localization of Light. *Phys. Today* **1991**, *44*, 32–40. [[CrossRef](#)]
52. Andreasen, J.; Asatryan, A.A.; Botten, L.C.; Byrne, M.A.; Cao, H.; Ge, L.; Labonté, L.; Sebbah, P.; Stone, A.D.; Türeci, H.E.; et al. Modes of random lasers. *Adv. Opt. Photon.* **2011**, *3*, 88–127. [[CrossRef](#)]
53. Segev, M.; Silberberg, Y.; Christodoulides, D.N. Anderson localization of light. *Nat. Photon* **2013**, *7*, 197–204. [[CrossRef](#)]
54. Meulenkamp, E.A. Synthesis and Growth of ZnO Nanoparticles. *J. Phys. Chem. B* **1998**, *102*, 5566–5572. [[CrossRef](#)]
55. Meulenkamp, E.A. Size Dependence of the Dissolution of ZnO Nanoparticles. *J. Phys. Chem. B* **1998**, *102*, 7764–7769. [[CrossRef](#)]
56. McCluskey, M.D.; Jokela, S.J. Defects in ZnO. *J. Appl. Phys.* **2009**, *106*, 071101. [[CrossRef](#)]
57. Janotti, A.; Van de Walle, C.G. Oxygen vacancies in ZnO. *Appl. Phys. Lett.* **2005**, *87*, 122102. [[CrossRef](#)]
58. Srikant, V.; Clarke, D.R. On the optical band gap of zinc oxide. *J. App. Phys.* **1998**, *83*, 5447–5451. [[CrossRef](#)]